

Article

Does Particle Size in Nanofluid Synthesis Affect Their Performance as Heat Transfer Fluid in Flat Plate Collectors?—An Energy and Exergy Analysis

Ayomide Titus Ogungbemi ¹, Humphrey Adun ^{1,*}, Michael Adedeji ¹, Doga Kavaz ² and Mustafa Dagbasi ¹¹ Energy Systems Engineering Department, Cyprus International University, Mersin 10, Nicosia 99258, Turkey² Bioengineering Engineering Department, Cyprus International University, Haspolat-Lefkosa, Mersin 10, Nicosia 99258, Turkey

* Correspondence: hadun@ciu.edu.tr

Abstract: A flat-plate collector is one of the most common solar collector systems due to its comparatively lower cost and maintenance. However, the performance of this type of collector is low; thus, research studies in the past decades have focused on improving its efficiency through various plate configurations and efficient working fluids. This study recognizes the research gap regarding the influence of nanoparticle shapes and their effects on improving the heat transfer properties in flat-plate collectors. In this study, fly ash nanofluid at 0.5% (with a range of nanoparticle sizes) was used as a working fluid to investigate the performance of a flat-plate collector. This study analyzed the behavior of the collector system via a range of Reynolds numbers in its laminar regime, between 800 and 2000. The results measured in this study showed that the maximum energy efficiency measured was 73.8%, which was recorded for the fly ash nanofluid at a nanoparticle size of 11.5 nm. At a Reynolds number of 2000, the fly ash nanofluid with a nanoparticle size of 11.5 nm showed a top heat loss coefficient of 4.78 W/m²K, while the top heat loss coefficient of a nanoparticle size (NPS) of 114 nm was 5.17 W/m²K. This study provides a framework for the significance of the nanoparticle size in the synthesis of nanofluids in both mono and hybrid composites and application in solar collector systems.

Keywords: flat-plate collector; nanofluid; Reynolds number; nanoparticle size

check for updates

Citation: Ogungbemi, A.T.; Adun, H.; Adedeji, M.; Kavaz, D.; Dagbasi, M. Does Particle Size in Nanofluid Synthesis Affect Their Performance as Heat Transfer Fluid in Flat Plate Collectors?—An Energy and Exergy Analysis. *Sustainability* **2022**, *14*, 10429. <https://doi.org/10.3390/su141610429>

Academic Editor: Sergio Nardini

Received: 19 July 2022

Accepted: 19 August 2022

Published: 22 August 2022

Publisher's Note: MDPI stays neutral with regard to jurisdictional claims in published maps and institutional affiliations.



Copyright: © 2022 by the authors. Licensee MDPI, Basel, Switzerland. This article is an open access article distributed under the terms and conditions of the Creative Commons Attribution (CC BY) license (<https://creativecommons.org/licenses/by/4.0/>).

1. Introduction

The rapid growth of the global population and advances in civilization have resulted in exponential growth in energy demand. Although fossil fuels are not sustainable and have severe environmental and health problems [1,2], they are still the main contributors to the energy sector. Greenhouse gases, such as methane, carbon dioxide, and nitrous oxide are emitted in large quantities during the combustion process of fossil fuels. It is also expected that the emissions of these gases will increase in time due to the rapid rate of civil and industrial growth. Over the years, governments and private institutions have implemented both policy formulations and renewable energy productions to meet growing energy demands. The share of renewable energy in global power production has increased throughout the years, as depicted in Figure 1. It is seen that, despite the continued use of fossil fuels (owing to factors, such as cost), renewable energy production experienced a 60% increase between 1990 and 2019. The share of coal in power generation increased between 1990 and 2015, and there has been a gradual decrease. However, the share of oil in power generation has been on the decline since 1990. Figure 1 also shows that the share of low carbon sources has been increasing since 2008. A secure and decarbonized power system needs other flexible resources on a far greater scale than what is now available because solar PV and wind power are unpredictable. Low-carbon dispatchable power plants are among them. High proportions of low-carbon hydrogen and ammonia can be

burned in fossil fuel power plants, giving countries other options for decarbonizing the energy sector. The corresponding technologies are developing quickly. Small power plants have successfully co-fired up to 20% ammonia and over 90% hydrogen, and larger-scale test projects with higher co-firing rates are in the works. In the shift to renewable energy, low-carbon hydrogen and ammonia can be used in fossil fuel power plants to ensure electrical security. Several factors, including the market structure, the accessibility of other flexible choices, the composition of the energy mix, and the price of carbon, which can differ significantly among areas, influence the value of low-carbon dispatchable power capacity (IEA, 2021).

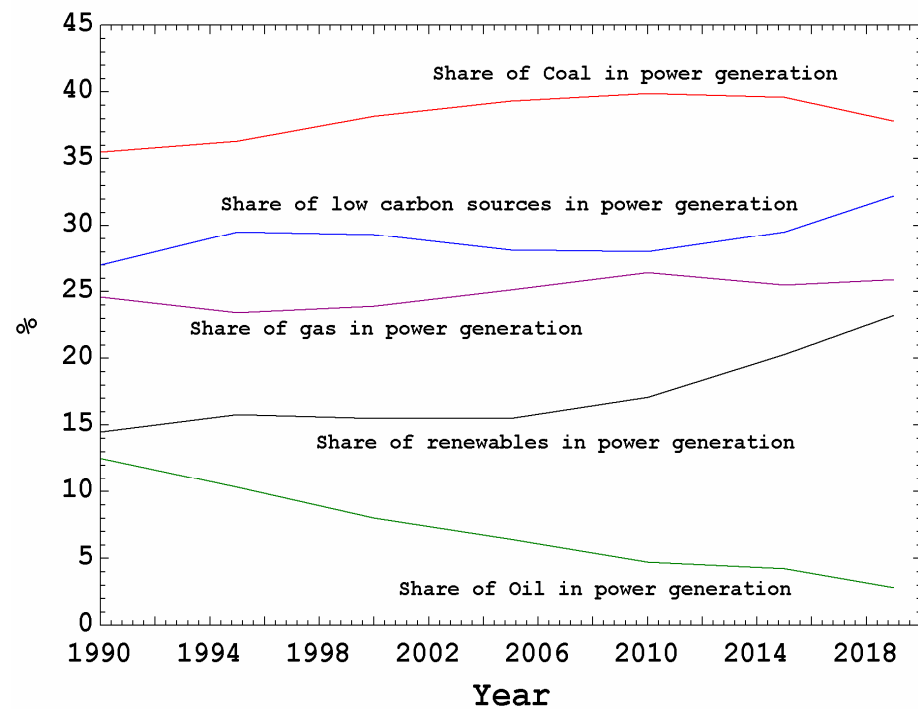


Figure 1. Share of renewables and fossil fuels in global power generation.

Amongst renewables, solar energy presents the best alternative as it is abundant in most regions in the world, and solar technologies are becoming economically competitive in the global energy market [3]. The most common solar technology is the solar flat-plate collector, due to its cheap cost and ease of installation [4]. The operation of a flat-plate collector (FPC) involves the absorption of heat through its body, and then the heat absorbed is transferred to the heat transfer fluid. The performance of an FPC is subject to factors, such as climatic conditions, the configuration of the FPC, mass flux rate, and type and properties of heat transfer fluids. In this study, the focus is on analyzing the intricate details of the heat transfer fluid (nanofluid). The unique properties of nanofluids, such as low heat capacity, thermal conductivity, and heat transfer properties, make them show better heat absorbing properties as compared to other conventional fluids, such as water, oil, etc. Apart from their heat transfer properties, the effects of the scattering properties of nanofluids have received some research attention. The study by Xingyu et al. [5] analyzed the improvement of solar absorption performance of nanoparticles by varying the scattering effects of nanoparticles and incident light locations. Their study, which measured the outputs, such as absorbance, reflectance, and transmittance, showed that the absorbance of nanoparticle suspension could be improved by enhancing its scattering ability. Their study also specifically measured a maximum solar absorption efficiency of 94.4% at $d = 1$ cm, which was 5.7% higher than at $d = 0$ cm. Moreover, a similar study by Xingyu et al. [6] investigated the solar absorption performance of the copper@carbon core-shell. Their study showed that the optimal absorption power per unit volume was measured for core radius

and shell thickness of 25 and 4 nm, respectively, while the maximum solar absorption of 95.6% was measured for core radius and thickness of 25 nm and 14 nm, respectively. Their study concluded that the optical properties of the copper@carbon nanoparticle were significantly affected by their radius and shell thickness. The study by Chen et al. [7] specifically experimented with plasmonic nanofluids and stated that by tuning their shape and size, they can absorb and transmit a specific spectrum.

The research bank of nanofluids [8–10], and their applications in collector systems, have presented defining conclusions, in terms of their performance. Different factors, such as nanoparticle type [11], base fluids used in nanofluid synthesis [12], nanoparticle shapes [13–15], the combination of nanoparticles [16], and nanoparticle sizes [17] affect their heat transfer properties, especially in FPC applications. Experimental and numerical studies have been conducted to show the effects of these nanofluid factors on the performance of the FPC. In a study by [18], carbon-based–graphene oxide nanofluid was prepared at a mass fraction between 0.10 and 0.45% and a temperature range between 25 and 50 °C. The nanofluid was used as a working fluid in a FPC, and their results showed that the temperature of the riser tube of the FPC decreased with increased mass fraction and temperature of the nanofluid. The effect of utilizing hybridized nanofluid against one particle nanofluid on the performance of a FPC was investigated in a study by [19]. Their study showed that the optimum energy efficiency using an $\text{Al}_2\text{O}_3\text{-Cu}$ /water hybrid nanofluid compared to Al_2O_3 /water and water was 3.86% and 4.23%, respectively. Their study also investigated the environmental benefits of the nanofluid-based system and measured maximum reductions of CO_2 , SO_2 , NO_2 of 29.15, 0.0149, and 0.0255 kg compared to water. A similar study that compared the performances of mono and hybrid nanofluid-based collector systems was conducted by [20]. Their study utilized SiO_2 /Cu hybrid nanofluids, alongside SiO_2 and Cu mono nanofluids. Their results showed that the maximum thermal performance was measured for the 5% Cu/water mono nanofluid. It is worth noting—based on their results and other supporting research—that despite the overwhelming support for better thermophysical properties of hybrid nanofluids, compared to mono nanofluids, the volume fraction of each nanoparticle in the composite has a significant effect on the performance. A study by [4] carried out an experimental and numerical analysis of an FPC system using alumina nanofluids with varying volume fractions and compared the results with the water-based FPC system. Their study showed that the optimal thermal performance was calculated at a volume fraction of 0.5%; increasing it above that threshold resulted in a negative effect on the FPC system. A study by Ovais et al. [21] investigated the stability and rheological behavior of $\text{Al}_2\text{O}_3\text{-TiO}_2$ thermol-55 nanofluids for the solar collector. Their study synthesized the hybrid nanofluid at the range of volume concentration between 0.05 and 0.5 wt%. Their results showed that the synthesized hybrid nanofluid showed viable properties as heat transfer fluid in the collector systems, due to the insignificant viscosity increase at the higher temperature. A similar result was measured in the study by Ovais et al. [22]; their study synthesized $\text{Al}_2\text{O}_3\text{-TiO}_2$ using oleic acid as a surfactant.

Some studies have also investigated the effects of nanoparticle shapes on the performance of the FPCs, such as the study by [23]. In their study, boehmite–alumina nanoparticles with different shapes of bricks, platelets, blades, and cylinders were used in synthesizing the water-based nanofluid, and applied as a heat transfer fluid in a hexagonal cross-sectional tube of the FPC. Their study, which considered varying properties, such as volume fraction, flow rate, and temperature, numerically measured that the maximum increase in the outlet temperature of the FPC was noticed for the brick-shaped nanoparticle.

As seen in the literature, there is a concentration of research on hybridized nanofluids and their impacts on the performances of solar collector systems. This study attempts to cover the research gap by investigating the effects of the particle sizes of nanofluids. A study by [24] experimentally showed that the thermal conductivity of nanofluids increased as the nanoparticle size (NPS) decreased. A similar investigation of the effect of the NPS on the thermal conductivity of Al_2O_3 , ZnO, and TiO_2 nanofluids was made by [25]; their study conclusively corroborated the increase in thermal conductivity with a decrease in the

NPS. Their study further measured that there was a thermal conductivity amplification of 16% for a 10 nm-sized nanoparticle as compared to a 70 nm sample, at a volume fraction of 3% TiO_2 . The possible reason for the enhancement of thermal conductivity with a decrease in the nanoparticle size was stated in a study by Das [26]. Their study, which synthesized Al_2O_3 /water and Al_2O_3 /Ethylene Glycol (EG) nanofluids, revealed that the enhanced surface to volume of smaller-sized nanoparticles caused the amplification of thermal conductivity of smaller-sized particles. A study by Esfe et al. [27] also experimentally measured an increase in thermal conductivity with the decrease in the NPS; their study attributed this behavior to a larger interfacial region between the particles and the base fluid. A contrary result was measured in the study by Xia et al. [28], which studied the Al_2O_3 nanofluid at sizes of 13 and 20 nm. Their study mentioned that, in some situations, the thermal conductivity of nanofluids was not affected by the decrease in NPS. This was also corroborated in the study by Beck et al. [29], which synthesized Al_2O_3 nanoparticles from 8 to 282 nm. Their study showed that the decrease in NPSs also caused a decrease in thermal conductivity for nanoparticles with sizes lesser than 50 nm, while for larger nanoparticle sizes, the decrease in NPS did not significantly affect the thermal conductivity. A different result was retrieved in a study by Timofeeva et al. [30]. Their study, which synthesized SiC nanofluid at particle sizes of 16 to 90 nm, reported an increase in thermal conductivity with an increase in NPS. Furthermore, the effect of the NPS on viscosity also showed conflicting results, such as that of thermal conductivity. The increase in viscosity, with an increase in the NPS, was reported in studies by [31–33]. The contrary result of increasing viscosity with a decrease in the NPS was experimentally retrieved in studies by [34,35]. The specific heat capacity (SHC) is a property that affects how much energy is required to raise the temperature of a fluid. The SHC of nanofluids is an important property as it affects their thermal storage and heat transfer characteristics. The sizes of nanoparticles also affect the specific heat capacities of nanofluids, as shown in a study by Angayarkanni et al. [36]. Their study measured the SHC of magnetite, alumina spheres, and alumina nanorods. Their results showed that the SHC of the nanofluids decreased with an increase in the nanoparticle size of the kerosene-based magnetite, but for the polyalphaolefin-based alumina nanofluid, the SHC increased with the increasing nano size. Their study concluded that the SHC decrease based on the aspect ratio of nanoparticles was attributed to reduced surface atomic contributions. Moreover, a robust study on the influence of nanoparticle sizes on the SHC of nanosalts was investigated by Bharath et al. [37]. Their study was built on the improvement in research regarding the enhancement of SHC of nanosalts for heat transfer and storage applications. Their study experimentally synthesized different sizes of SiO_2 (5, 10, 30, 60 nm), and dispersed them in NaNO_3 and KNO_3 salts. Their study results showed that the SHCs of the nanosalts were enhanced by 8%, 12%, 19%, and 27% for nanosizes of 5, 10, 30, and 60 nm, respectively. Hamed et al. [38] noted in their study that contradicting results have been recorded in the literature concerning the effects of nanoparticle sizes on the SHC of nanofluids. They found that stable dispersions increased the specific heat of solar salt by 17.6%, whereas inadequate particle dispersion can decrease the specific heat capacity of molten salts. Therefore, it is crucial to closely monitor the preparation processes and particle dispersion to accomplish a particular heat increase of nanosalts. Other studies [39,40] have also proven the significant effects of nanoparticle sizes on the SHCs of nanofluids and in turn their impacts on solar technology systems.

The contradictory and conflicting results in the discourse on the effects of particle sizes on thermophysical properties under similar conditions is a research gap that needs to be filled through more experimental and numerical analyses. Moreover, very few studies have considered examining the performances of solar collector systems based on the nanoparticle sizes of mono or hybrid nanofluids. This is an even more significant research path considering that the economic costs of synthesizing nanofluids hinges on nanoparticle size synthesis. Therefore, for the large-scale application of nanofluids as heat transfer fluids, the optimal nanoparticle size is required for efficient operation. The consideration of the

NPS, as it affects its application in the thermal system, has received some research attention. A study by [41] numerically investigated the performance of a radiator under varying conditions of NPSs. Their study synthesized Ag nanoparticles at sizes from 20 to 100 nm, at temperatures between 35 and 75 °C. The findings indicated that nanoparticles with smaller-sized diameters had better thermophysical characteristics than large nanoparticles. Measurements were made of the friction factor features and heat transfer properties. Ag exhibits superior thermal conductivity at 20 nm compared to other nanofluids, indicating that smaller nanoparticles can reduce the radiator size and enhance thermal conductivity. Nanofluid properties ‘studying’ their impacts on FPCs are shown in Table 1.

The effect of particle shapes on the performances of flat-plate collectors was studied by [42]. Moreover, the effect of pH on the performances of flat-plate collectors was investigated by [43]. These two studies present different performances of solar collectors on the variables of the synthesis process of nanofluids. This requires even more research attention as the process of nanofluid synthesis is becoming more complex with hybrid and ternary nanofluids. The effect of nanoparticle size is even more critical to study considering the contradiction of different authors regarding their thermophysical properties. Table 1 shows that most research on the FPC performance with a nanofluid concentrate was mainly on the volume concentration of nanoparticles, leaving other synthesis parameters with less research attention. This study covers that gap.

This study will serve as a contribution to the continuing search to solidify the effects of nanoparticle sizes on thermophysical properties, and their influence in applications (e.g., as heat transfer fluids). Moreover, to the best of our knowledge, no study has investigated the application of fly ash nanoparticles as a working fluid in a solar collector system. This study will retrieve thermophysical properties from the experimental analysis of [44], which considered various nanoparticle sizes as working fluid in the designed solar collector system.

Table 1. Nanofluid properties studied concerning their FPC impacts.

Reference	Nanofluid Synthesized	Nanoparticle Property Considered	Range of Factor	Results
[43]	MWCNT/H ₂ O	PH variation	3.5, 6.5, 9.5	Their results show that enhancing the performance of the FPC arises with more difference between the PH of the nanofluid and the PH of the isoelectric point.
[45]	MWCNT/water, graphene/water, copper oxide/water, aluminum/water, titanium oxide/water, and silicon oxide/water	Nanoparticle type, volume fraction	0.25%, 0.5%, 0.75%, 1.0%, 1.5%, and 2.0% for each nanoparticle type	Their results showed that the optimum collector efficiency was measured for 0.75 wt % MWCNT/water.
[46]	Metal oxides	Nanoparticle type	CuO, SiO ₂ , TiO ₂ , and Al ₂ O ₃ nanofluid	CuO showed the maximum thermal efficiency due to its lower SHC.
[47]	Single-walled carbon nanotubes	Volume fraction	0.1%, and 0.3%	The maximum efficiency of the collector was measured for the 0.3% volume fraction.
[48]	Al ₂ O ₃ /water 12 nm particle size	Volume fraction Surfactant	0.2%, and 0.4%, With and without surfactant	Their results showed that the efficiency of the FPC was higher with the nanofluid synthesized using a surfactant. Moreover, the performance of the FPC was higher in the 0.4% volume fraction.
[42]	Al ₂ O ₃	Nanoparticle shape	Platelets, blades, cylindrical, bricks, spherical	Their study showed that the blade-shaped nanoparticle gave the highest collector efficiency.
[49]	Multi-walled carbon nanotubes	Outside diameter of Nanoparticles	<8 nm with SSA of 500 m ² /g, and 20–30 nm with SSA of 110 m ² /g	Their study showed that the nanoparticle with an outside diameter of <8 nm gave a distinguishable result in terms of the FPC performance.
[23]	boehmite-alumina	Nanoparticle shape	Bricks, cylinder, platelets, blades	Their study showed that brick-shaped nanoparticles gave the maximum outlet temperature from the collector, while platelet-shaped NPs gave the least.

2. Materials and Methods

2.1. Mathematical Modeling of the FPC

Simple logic underlies the solar flat-plate collector. To turn solar radiation energy into heat energy, a dark, flat surface called an absorber sheet or plate must first be heated. The fluid passing through the pipes connected to the absorber sheet receives this heat transfer after that. To maximize the absorption of incident solar radiation, the absorber sheets are painted with selective coatings and constructed of high thermal conductivity metals, such as copper, aluminum, or steel. Reduced heat losses from the chosen surface come from the use of a transparent glass cover.

The fluid-transporting tubes or ducts are either built into or connected to the absorber sheets [50]. In this study, the effect of the nanoparticle size and configuration of base fluid on a flat-plate collector is investigated. Figure 2 shows the schematic diagram of a flat-plate collector. The details of the collector system are presented in Table 2. For the context of this study, certain assumptions are made.

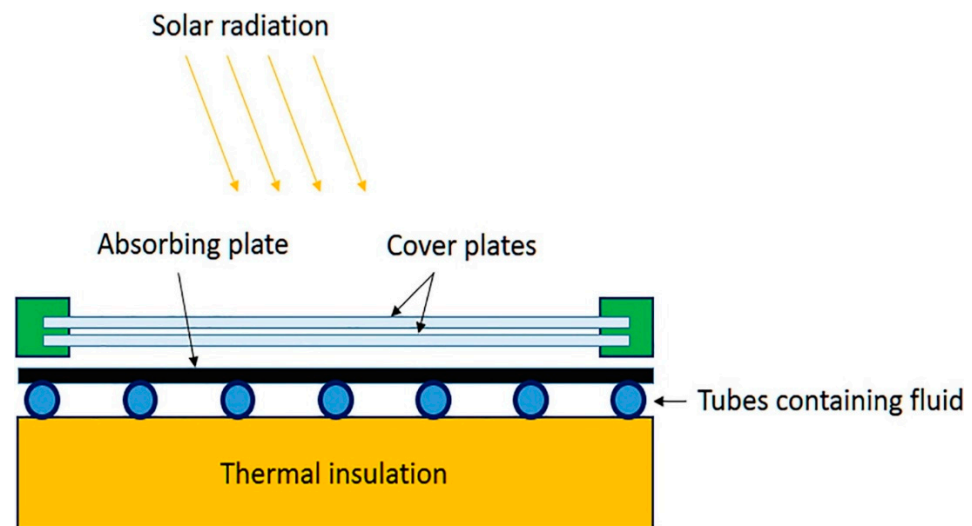


Figure 2. Schematic of a flat-plate collector (FPC).

Table 2. FPC parameters used in this study.

FPC Parameters	Specifications
Area of collector	2 m ²
Collector length	2 m
Collector width	1 m
Collector height	0.15 m
Tilt angle of collector	15
Thickness of back insulation	0.05 m
Thickness of edge insulation	0.025 m
Thickness of absorber plate	0.00045 m
Absorber plate's thermal conductivity	386 W/m k
Absorber plate's emissivity	0.95
Effective transmittance-absorptance product	0.82
Glass cover's thickness	0.004 m
Glass cover's absorptivity	0.05
Glass cover's emissivity	0.88
Tube spacing between risers (9 nos)	0.095 m
Inner diameter of the riser pipe	0.0095 m
Outer diameter of the riser pipe	0.01 m
Diameter of header pipe	0.0254 m

The heat transfer fluid used in the FPC assumed a laminar flow. The reason for the choice of laminar is based on the better exergy efficiency that is retrieved for the laminar

flow compared to the turbulent flow regime [51]. The flow within the channel has a Reynolds number that ranges between 800 and 2000. The configuration of the FPC used was patterned according to the experimental setup from the study by [19]. The following assumptions were taken into account to condense the 3D coupled heat transfer and fluid flow problem into a straightforward 2D transient mathematical model;

- The effect of dust on the FPC was neglected.
- The thermal capacitance of the FPC was not considered.
- The front and back of the FPC were assumed to have the same temperature.
- The assumption of a one-dimensional perpendicular to the flow region in terms of the heat transfer was made.
- Consideration was given to the rear insulation's natural convection with the surrounding air.
- Losses from radiation and convection from the insulation's bottom and side surfaces were negligible.
- The translucent cover blocked off infrared light. It was assumed that the physical characteristics of materials were unaffected by changes in temperature.
- The insulation materials, absorber, and glass cover were not affected by temperature change.

2.2. Mathematical Modeling

The operation of the flat-plate collector involves the utilization of the solar radiation, by the heat transfer fluid, which is first received by the absorber plate. It is worth stating that not all of the radiation reaching the absorber plate was used due to heat loss from the absorber material. Therefore, to compute the useful energy (Q_u) entering the heat transfer fluid, Equation (1) is used [45]:

$$Q_u = A_c [S - U_L (T_{pm} - T_a)] \quad (1)$$

where the collector area is represented by A_c , the plate temperature, ambient temperature, and total coefficient of heat loss are represented by T_{pm} , T_a , and U_L , respectively. In estimating the total heat loss coefficient, the top, edge, and bottom losses need to be accounted for as depicted in Equation (2) [45]:

$$U_L = U_t + U_b + U_e \quad (2)$$

To decrease the heat loss from the collector system, which would increase the performance of the system, insulation is incorporated into the bottom and sides of the collector. Equations (3) and (4) give the mathematical computations of the heat loss from the bottom and side of the collector:

$$U_b = \left(\frac{L_b}{K_b} + \frac{1}{h_{b,a}} \right)^{-1} \quad (3)$$

$$U_e = \left(\frac{L_e}{K_b} + \frac{1}{h_{b,e}} \right)^{-1} \frac{A_e}{A_c} \quad (4)$$

where L_b , K_b , $h_{b,a}$ represent the thickness of the bottom of the collector, thermal conductivity of the material used for the bottom collector, and convection heat transfer at the collector's bottom. The thickness of the collector's side and heat convection at the side of the collector are represented by L_e , and $h_{b,e}$ respectively.

The fin analysis was used in this study to estimate the effectiveness of the collector system. The heat transfer fluid absorbed the heat as it flowed through the tubes exposed to the irradiation. References [52,53] give the computational analyses of the fin analysis methodology. In estimating the average plate temperature, Equation (5) is used [49]:

$$T_{pm} = T_i + \frac{\dot{Q}_u}{A_c \times U_L \times F_R} \times (1 - F_R) \quad (5)$$

where the inlet temperature and heat transfer factor are represented using T_i and F_R , respectively. A constant value of 305.15 K is used as the inlet temperature in this study. To compute the heat transfer factor, Equation (6) is used [42]

$$F_R = \frac{\dot{m}C_p}{A_c U_L} \left[1 - \exp\left(\frac{-A_c \times U_L \times F'}{\dot{m}C_p}\right) \right] \quad (6)$$

where the \dot{m} and C_p are used to depict the mass flow rate in kg/s and specific heat capacity of the working fluid. The coefficient of collector efficiency is represented using F' , which can be calculated using Equation (7) [42]

$$F' = \left(w \left[\frac{1}{(D + (W - D)F)} + \frac{U_L}{\pi D_i h_{fi}} \right] \right)^{-1} \quad (7)$$

The W and D represent the distance from the center to the center of the fluid carrying the tubes, and the outer diameter of the tube, respectively [50]

$$F = \frac{\tanh(m(W - D)/2)}{(m(W - D)/2)} \quad (8)$$

The computation of the energy efficiency of the flat-plate collector is made by dividing the output energy with the available input solar irradiation, as shown in Equation (9), where the G_T represents solar radiation [54]

$$\eta = \frac{Q_u}{A_c G_T} \quad (9)$$

Standards used in evaluating the flat-plate collector systems involve the minimization of the pressure drop and maximization of the ratio of heat transfer to the pressure drop.

Considering that in the solar collector system, the risers are parallel, the major head loss is represented as

$$h_{1,major} = h_{1,riser1} = h_{1,riser2} = \dots h_{1,risern} \quad (10)$$

The sum of the major and minor head losses gives the total head loss, h_L :

$$h_L = h_{1,major} + h_{1,minor} = \frac{8\dot{m}_r^2}{\rho^2 g \pi^2 D_i^4} \left(f \frac{L_r}{D_i} + \sum K_L \right) \quad (11)$$

where the loss coefficient is represented as K_L [55] (which is represented as 1 in turbulent flow, and 2 for laminar flow), and the length of the riser is represented as L_r . In obtaining the pressure drop, the inlet and outlet of the riser is used in formulating the energy equation. Considering the constant velocity of the inlet and outlet of the riser, the energy equation is:

$$\frac{P_1}{\rho g} + z_1 = \frac{P_2}{\rho g} + z_2 + h_L \quad (12)$$

The vertical distance between the inlet and outlet of the riser is represented by the $z_2 - z_1$, the slope angle of the collector is explained by β , and the $L \sin \beta$ gives the vertical distance; therefore, $z_2 - z_1 = L \sin \beta$. The pressure drop of the collector is then estimated by

$$\Delta P = P_1 - P_2 = \rho_f g (L \sin \beta + h_L) \quad (13)$$

The analysis of the pumping power is important, especially as it informs the comparison

with the base fluid. It also affects the cost of utilizing each system, as the cost of the pumps can be ascertained. Equation (14) shows the mathematical formulation

$$W_p = \dot{m} \frac{\Delta P}{\rho_f} \quad (14)$$

Since both the heat transfer and the pressure drop rise when using the nanofluid, the results of the heat transfer and pressure drop cannot be used separately to contain the accurate conclusion that employing the nanofluid is a suitable alternative. As a result, in addition to the h/pressure drop, a comprehensive assessment element known as the performance evaluation criteria (PEC) was developed [56]. The PEC is computed using Equation (15), at constant pumping power and pressure drop, respectively [57].

$$PEC = \frac{Q_u}{V \Delta P} \quad (15)$$

2.3. Fly Ash Particles

Considering the increase in the global energy demand, and the corresponding consumption of coal to meet global energy requirements, there has been a concurrent increase in fly ash production. Fly ash is a combination of porous spheroids of mainly elemental carbon and inorganic ash spheres derived from the combustion of fossil fuels at a temperature of about 1750 °C and a heating rate of 104 °C/s. Fly ash is divided into three components based on different formations; which are non-combustible material (IASs), combustible matter not burned (SCP), and the fly ash formed during the combustion process [58]

The large discharge of fly ash has significant environmental and health damage due to the presence of surface-bound hydrocarbons and toxic materials. These toxic metals, such as Cu, Pb, Cd, and Ni in fly ash, hurt aquatic and terrestrial ecosystems. A recent discovery by [59] stated that transition metals in oil fly ash also cause damage to DNA cells. Fly ash has been used as raw material for making concrete in the cement industry. In addition, fly ash from thermal power plants is a used byproduct in agricultural and engineering reutilizing materials.

However, despite the studies on fly ash in the literature, there is limited information on fly ash nanoparticles as it relates to their characterization.

2.4. Description of Nanoparticles/Nanofluids Used in This Study

The choice of nanofluids used in this study is based on the research gap and the objective of the study. The nanofluids utilized in this study are fly ash nanofluids at varying nanoparticle sizes, as were retrieved in the study by [44].

The fly ash nanofluid was synthesized using its corresponding nanoparticles, using water as the base fluid. Triton X100 was used as a surfactant to ensure the stability of the mixture. In the synthesis of the fly ash nanofluid, a high-energy balling technique was used, which resulted in producing fine particles of the nanoparticles in a short time. The fly ash particles, which were spherical, went through further sieving before being ball-milled to yield particle sizes of 11.5, 30.36, 55.5, 89, and 114 nm. The process of determining the nanoparticle size was conducted using a dynamic light scattering analyzer (DLS) and SEM analysis. The fly ash nanofluid was prepared using the two-step method at a volume fraction of 0.5%. The mixture of the nanoparticles, base fluid, and surfactant was stirred for about 30 min in a magnetic stirrer and then sonicated for 3 h in an ultrasonicator. The stability of the prepared nanofluid was analyzed using sedimentation, Zeta analyzer, transmission electron microscopy (TEM), UV-Vis spectrophotometer, and the DLS method. The stability test showed that the fly ash nanofluid had good stability (with values above 46.5 mv); however, the stability reduced as the particle size increased. The thermal conductivity and viscosity properties were measured using a KD2 pro-thermal property analyzer and LVDV-II+Pro Brookfield programmable digital viscometer, respectively.

The DLS method was used to measure the size distribution of the fly ash nanoparticles. In the x-ray analysis, the metal oxides found in the fly ash sample were SiO₂ (61.29%), Al₂O₃ (26.6%), Fe₂O₃ (6.12%), TiO₂ (2.08%), and MgO (1.94%). Figure 3 also shows the average particle size at different ball milling times as presented in the study by [44]

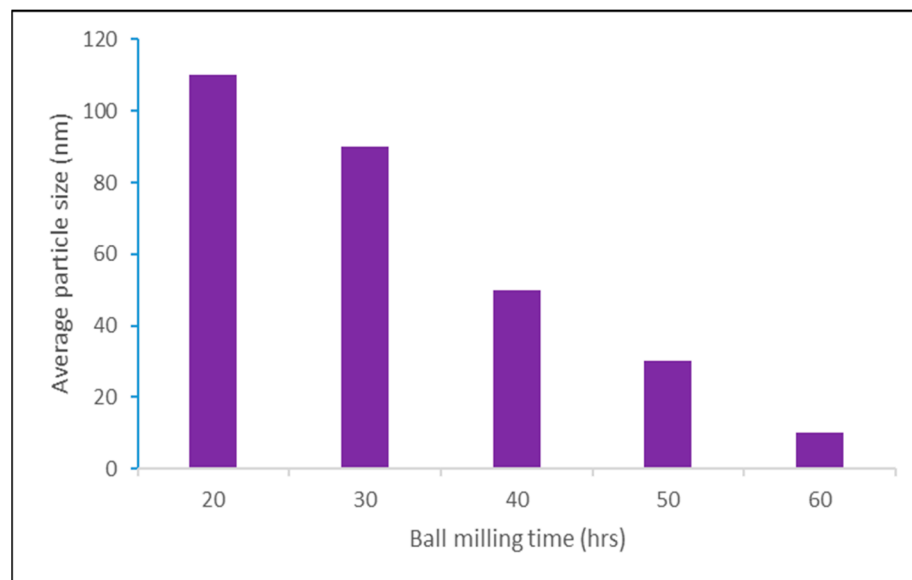


Figure 3. Balling time vs. average particle size.

In the preparation of the nanofluid, the two-step method was used. A total of 0.5% of the fly ash nanofluid was made using Equation (16). The appropriate nanoparticle was weighed and distributed in 100 mL of the base fluid (water). The mixture was stirred for 30 min using a magnetic stirrer to achieve stability. Afterward, the ultrasonicator was used to achieve even dispersion of the particles for about 3 h.

$$\text{Volume concentration, } \varphi = \frac{m_{np}/\rho_{np}}{m_{np}/\rho_{np} + m_{bf}/\rho_{bf}} \quad (16)$$

Thermophysical properties and Correlation Equations

For the numerical simulation of the model FPC designed for this study, the influences of the thermophysical properties (thermal conductivity, dynamic viscosity, specific heat capacity, and density) on the performance of the system were analyzed. This section discusses the behavior and thermophysical properties of the selected nanofluids.

The fly ash nanofluids showed increasing thermal conductivity as the nanoparticle size decreased and temperature increased. This trend is attributed to the improved Brownian motion in the base fluid for smaller-sized particles, as compared to larger-sized particles. In addition, the effect of a greater surface area on unit volume was also a reason for the better thermal conductivity of smaller-sized nanoparticles. According to a study by Pil et al. [60], where the role of the Brownian motion on enhanced thermal conductivity was conductivity, three theories were postulated (based on kinetics, Kapitza resistance, and convection). In regard to the nanoparticle size effect, the effect of thermal interactions of dynamic nanoparticles with the base fluid was discussed. At a macroscopic level, the interaction between liquid molecules and nanoparticles translates to conduction due to a lack of movement of bulk flow. However, at the nanoscale, it was postulated that the Brownian motion of nanoparticles produces a convection-like effect. Therefore, as the particle size reduces, the random motions of nanoparticles become larger, increasing the convection effect and, therefore, causing increased thermal conductivity [60]. Another possible reason for the increase in thermal conductivity with the decreasing nanoparticle size is the high nanofluid stability. The stability result of the nanofluid showed 46.5 mV,

36.5 mV, 34 mV, 31.5 mV, and 30 mV, for the 11.5 nm, 30.36 mV, 55.55 mV, 89 mV, and 114 mV, respectively. The results showed that the smaller-sized nanoparticles had greater stability. A study by Amin et al. [61] showed that increasing the ultra-sonication time caused an increase in the stability of nanofluids and thermal conductivity. This study agrees with their conclusion that the breaking down of larger clusters into smaller ones causes more homogenous suspensions of particles and, therefore, minimum agglomeration and higher stability/thermal conductivity. The results showed that the maximum thermal conductivity ratio (TCR) of the fly ash nanofluid was 1.12 at 60 °C, for the 11.5 nm sample. The least TCR of 1.01 (at 30 °C) was recorded for the 114 nm sample. The viscosity result of the nanofluid showed that as the nanoparticle size decreased, the viscosity enhanced. This observation could be attributed to higher interface resistance with the fluid layer, considering the larger surface area of smaller particles.

The correlation equations for the thermophysical properties for fly ash nanofluid are given in Equations (17)–(20).

$$k_{nf} = \left[0.9808 + 0.0142 * \phi_{np} + 0.2718 * \frac{T_{fm2}}{70} - 0.102 * \frac{PS_{np}}{150} \right] * k_{bf} \quad (17)$$

$$\mu_{nf} = \left[0.9042 + 0.1245 * \phi_{np} + 0.08445 * \frac{T_{fm2}}{72} - 0.06436 * \frac{PS_{np}}{170} \right] * \mu_{bf} \quad (18)$$

$$\rho_{nf} = (1 - \phi_{np}) * \rho_{bf} + \phi_{np} * \rho_{np} \quad (19)$$

$$Cp_{nf} = \frac{(1 - \phi_{np}) * \rho_{bf} * Cp_{bf} + \phi_{np} * \rho_{np} * Cp_{np}}{\phi_{np} * \rho_{np} + (1 - \phi_{np}) * \rho_{bf}} \quad (20)$$

2.5. Model Validation

The engineering equation solver (EES) was used to carry out the numerical analysis in this study.

The validation of the designed numerical model for this study was tested with the studies by [62] and [48]. The study by [62] was an experimental study that investigated the performance of solar flat-plate collectors under varying conditions of mass flow rates and different types of nanofluids. The parameters presented in their experimental analysis, such as collector configuration, mass flow rates, and loss coefficient, were inputted in the mode designed in this study. Table 3 presents the model results and their experimental outputs of the heat removal factor. The average error percentage was 0.9%, and the maximum error was 1.8%. A similar approach was used for the study by [48], which investigated the efficiency of flat-plate collectors on the changing conditions of volume fraction and mass flow rate. Table 3 also shows the error percentage between their experimental result and model computations of the heat removal factor. The maximum error calculated was 0.4%. These minimal errors show that the model developed in this study is accurate for making the numerical analysis to estimate the performance of the flat-plate collector in varying conditions of particle size effects.

Table 3. Model validation.

Mass Flow Rate (kg/min)	Weight Concentration (%) f-GNP	F_{RU_L} [62]	F_{RU_L} (Model Result)	Error Percentage (%)	Mass Flow Rate (L/min)	Weight Concentration (%) Al_2O_3	F_{RU_L} [48]	F_{RU_L} (Model Result)	Error Percentage (%)
0.8	0.1	6	5.89	1.867572	3	0.2	30.194	30.09	0.34563
	0.05	5.5449	5.53	0.269439					
	0.025	5.4050	5.35	1.028037		0.4	24.672	24.56	0.456026
1.2	0.1	6.3832	6.28	1.643312					
	0.05	5.9923	5.97	0.373534					
	0.025	5.9528	5.93	0.384486					

3. Result and Discussion

After ascertaining the accuracy of the model through the validation process, the performance of the flat-plate collector was investigated by numerically estimating parameters, such as the energy efficiency, exergy efficiency, heat loss coefficient, mean plate temperature, and fluid outlet temperature, and PEC values. It should be noted that the collector parameters displayed in Table 2 were used throughout the analysis. In addition, for all the performance criteria listed, the objective of this study was to investigate the influence of the particle size of the nanofluid.

Figure 4 presents the energy efficiency of the FPC with different nanoparticle sizes across the range of laminar flow regimes considered in this study. The volume concentration used in this study was 0.5%. The figure shows a general trend of increasing energy efficiency as the Reynolds number increases. This was due to an increase in convective heat transfer.

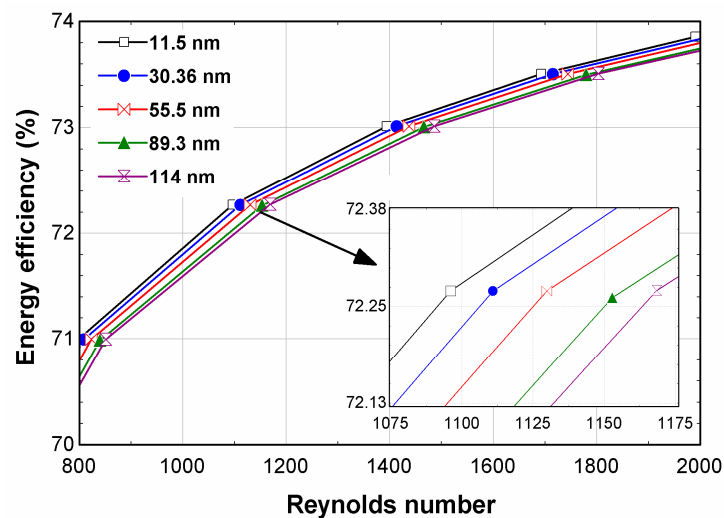


Figure 4. Energy efficiency of the FPC.

Moreover, the results show that the maximum energy efficiency measured was 73.8%, recorded for the 11.5 nm NPS. It was explained in a study by [63] that the Brownian–Reynolds number increases as the densities of nanoparticles decrease. The concept of Brownian–Reynolds was introduced by Prasher et al. [64], which was based on Brownian velocity and mathematically represented as $Re = \frac{1}{\nu} \sqrt{\frac{18K_B T}{\pi \rho d}}$, where ν and ρ represent the dynamic viscosity and density of the particles, respectively. The concept explains that with a decrease in the nanoparticle size, the Brownian–Reynolds number increases, and causes higher thermal conductivity and efficient photothermal conversion.

This suggests that smaller, lighter nanoparticles will have higher Brownian–Reynolds numbers and, thus, have higher thermal conductivity values. The least efficiency calculated was for the largest particle size of 114 nm. The maximum energy efficiency of the 114 nm fly ash nanofluid was 73.5%, which was 0.41% lesser than the 11.5 nm NPS at a Reynolds number of 2000. At a Reynolds number of 800, the energy efficiencies of 11.5 nm, 30.36 nm, 55.5 nm, 89.3 nm, and 114 nm were 71.3%, 71%, 70.72%, 70.67%, and 70.5%. Moreover, some studies have shown that the thermal conductivity of smaller-sized particles is higher than larger-sized particles owing to a larger interfacial region of the nanoparticles. This behavior can reflect in the heat absorption capacity of the smaller-sized nanoparticles, with better energy efficiency when used as a working fluid in flat-plate collectors. This result is corroborated by a study by [42], where nanoparticle sizes of 20 to 80 nm of alumina were tested on a flat-plate collector. Their study showed that a nanoparticle size of 20 nm gave optimum collector efficiency.

Exergy is the compact nature of a thermal system and is nothing more than the conversion of available energy into usable work. The exergy efficiency of the FPC is

depicted in Figure 5. Exergy efficiency, which is available energy to the system, showed a maximum efficiency for the smaller-sized particles. At a Reynolds number of 800, the efficiencies of 11.4 nm, 30.36 nm, 55.5 nm, 89.3 nm, and 114 nm were 1.964%, 1.975%, 1.989%, 2.005%, and 2.005%. The highest energy and exergy efficiencies of the smaller-sized nanoparticles were the result of higher thermal conductivity, which is supported by the thermophysical analysis result. The literature reports make it clear that the energy and exergy efficiencies frequently exhibit contradicting patterns. The collector's energy efficiency improves with the increasing mass flow rate and the Reynolds number, but this has the opposite effect on the collector's exergy efficiency. In the collector's absorber plate, the majority of the exergy destructions occur during the absorbing phase [47].

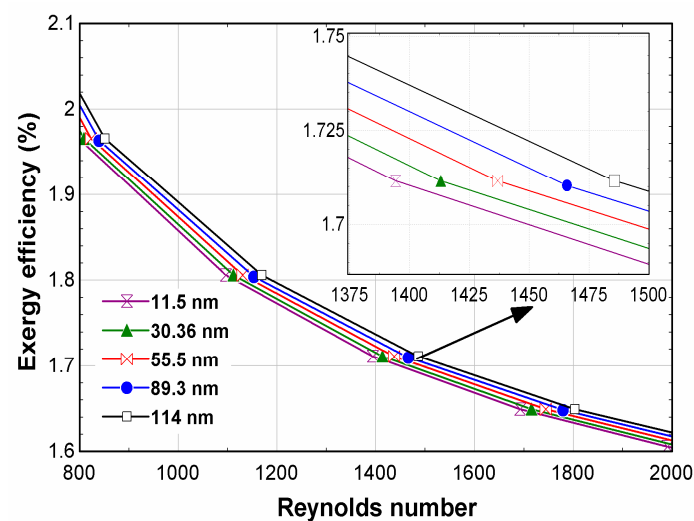


Figure 5. Exergy efficiency of the FPC at varying nanoparticle sizes.

The top and overall heat loss coefficients of the flat-plate collector were analyzed (presented in Figures 6 and 7). Since this study considered a constant inlet temperature, as there was no variation in the solar radiation received by the flat-plate collector, the variation in the energy efficiency is tied to the output energy from the collector, which is dependent on the heat loss. The heat loss from the top layer and the overall heat loss were computed (shown in Figures 6 and 7). Moreover, the output energy was dependent on the average mean plate temperature (presented in Figure 8).

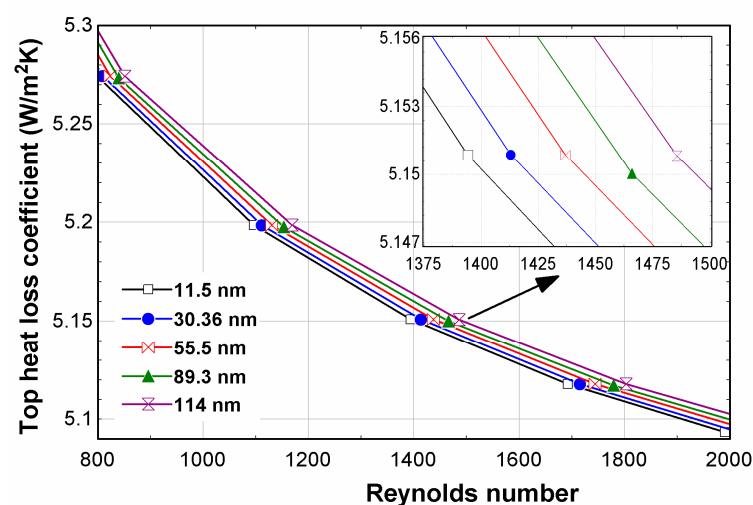


Figure 6. Top heat loss coefficient of the FPC.

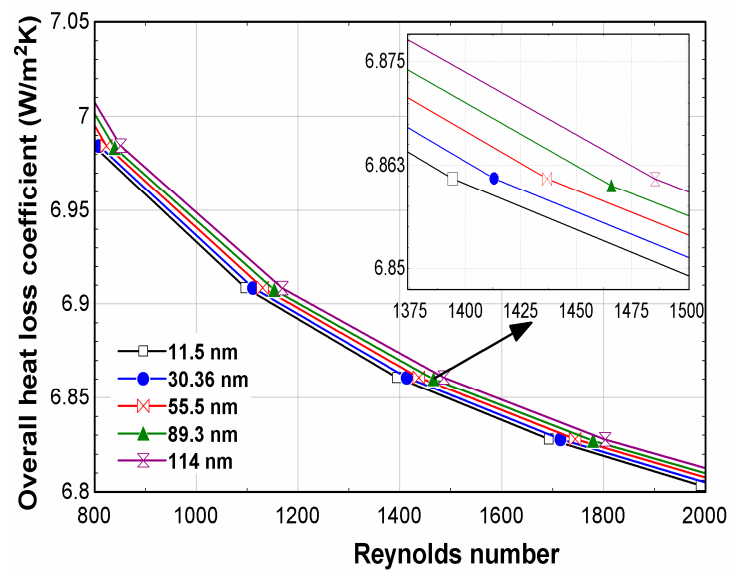


Figure 7. Total heat loss coefficient of the FPC.

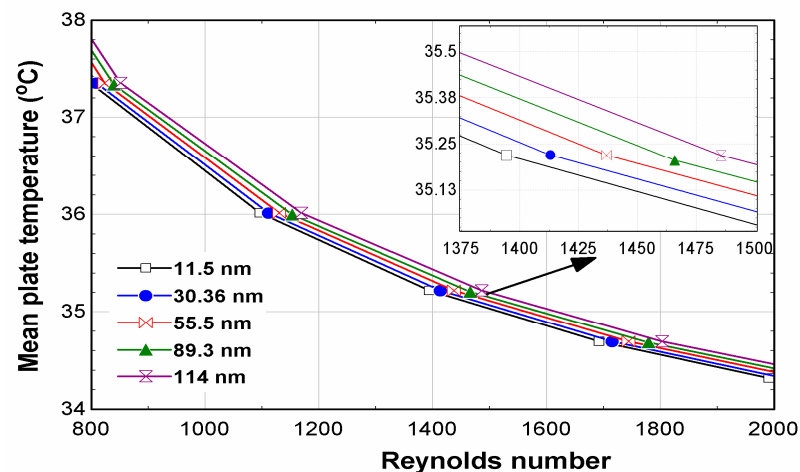


Figure 8. Mean plate temperature of the FPC with different NPS.

Figure 6 shows that the least heat loss measured was for the nanoparticle size of a 11.5 nm flash nanofluid. This explains the better energy output from the FPC. At a Reynolds number of 2000, the fly ash nanofluid with a nanoparticle size of 11.5 nm showed a top heat loss coefficient of $4.78 \text{ W/m}^2\text{K}$, while the top heat loss coefficient of NPS of 114 nm was $5.17 \text{ W/m}^2\text{K}$.

The overall heat loss coefficient of the FPC showed a similar trend as the top heat loss coefficient. The heat loss coefficient decreased with an increase in the Reynolds number. Figure 7 shows that a decrement of 2.57% was measured between the Reynolds numbers of 800 and 2000 for the 11.5 nm NPS. Decrements of 2.4%, 2.34%, 2.29%, and 1.78% were recorded for the Reynolds numbers of 800 and 2000 for 30.36, 55.5, 89.3, and 114 nm, which shows the maximum decrease measured for the fly ash nanofluid with a NPS of 11.5 nm. This decreasing trend of the heat loss coefficient with the increasing Reynolds number was attributed to the increase in the convective heat transfer of the working fluids. Moreover, the least overall heat loss of $6.8 \text{ W/m}^2\text{K}$ was recorded at 11.5 nm, while the maximum over heat loss of $7.1 \text{ W/m}^2\text{K}$ was measured at 114 nm.

The computation of the mean plate temperature of the FPC was made using Equation (5). Figure 8 shows that, at a lower Reynolds number, the mean plate temperature was higher, which also corresponded to a higher heat loss coefficient as noticed in Figure 8. This means that at a higher plate temperature, the possibility of heat loss from the FPC is higher,

due to a temperature difference with the environment (which can facilitate convection heat transfer). Figure 8 shows that at 800 and 2000 Reynolds numbers, the mean plate temperatures for 55.5 nm were 37.5 °C and 34.4 °C, respectively. Figure 8 also shows that as the nanoparticle size of the fly ash nanofluid increased, the mean plate temperature increased at a uniform Reynolds number. The numerical analysis measured the least and maximum mean plate temperatures (at a Reynolds number of 2000) at 34.21 °C and 34.57 °C, respectively. It is also worth stating that the trend of energy efficiency is an antithesis of the trends of the mean plate temperature and the heat loss coefficient. This means that with the decrease in the heat loss coefficient, the efficiency of the FPC increases. However, the heat removal factor is a crucial design parameter because it measures the amount of thermal resistance that solar radiation must overcome to reach the collecting fluid [65]. The increasing heat removal factor shown in Figure 9, as a result of the increase in the Reynolds number, is attributed to the decrease in the thermal resistance between the nanofluid and the wall of the collector [66]. The increase in the heat removal factor caused a decrease in the mean plate temperature, which increased the energy efficiency of the FPC. Figure 9 also shows that this increase in the heat removal factor was affected by the size of the nanoparticle used in the nanofluid synthesis. The fly ash nanofluid with the smallest nanoparticle size of 11.5 nm showed the highest heat removal factor. This was due to the higher thermal conductivity property of the smallest-sized nanoparticle. A study by [41], which investigated the thermal properties of different sizes of nanoparticles for the synthesis of the Ag nanofluid, corroborates the nanoparticle behavior in this study. Their study showed that the 20 nm of Ag nanofluid gave the highest thermal conductivity value compared to the 80 nm Ag nanofluid. The maximum heat removal factor was usually between 0 and 1, and it was recorded in this study that the least heat value of 8 was measured for 114 nm at a Reynolds number of 800. The heat removal factor for 11.5 nm had the highest value of 0.956 at a Reynolds number of 2000.

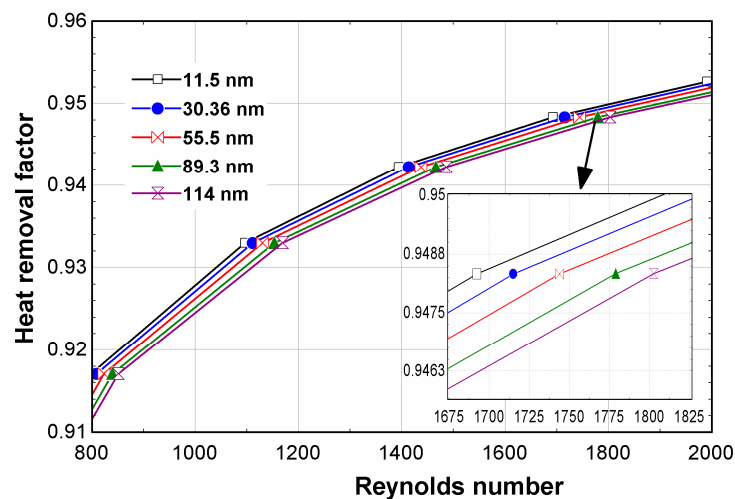


Figure 9. Heat removal factor of the FPC with different nanoparticle sizes.

The mean fluid temperature and fluid outlet temperature are shown in Figures 10 and 11. The temperature distribution inside the absorber plate along a flow direction was averaged mathematically to arrive at the mean fluid temperature. The mean fluid temperature of the fly ash nanofluid increased at increasing nanoparticle sizes. The mean fluid temperatures of the 114 nm NPS at Reynolds numbers of 800, 1000, and 2000 were 36.2 °C, 35 °C, and 32.5 °C. The fluid outlet temperature at an instantaneous solar irradiation condition will be affected by the heat removal factor and the heat loss coefficient. The maximum fluid outlet temperature was measured for the nanoparticle size of 114 nm. Moreover, as the Reynolds number increases, it can be seen that the difference in the mean fluid and outlet temperature of the different NPSs became more insignificant. This result is contradicted by a study by [67]. Their study investigated the effect of the nanoparticle size of aluminum

oxide in solar collectors and showed that the outlet temperature decreased as the NPS increased. However, their study mentioned that the decrease in outlet temperature was insignificant.

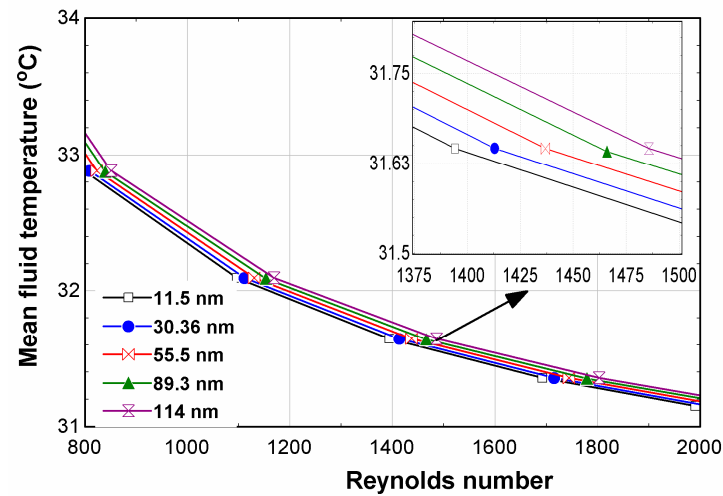


Figure 10. Mean fluid temperature of the FPC.

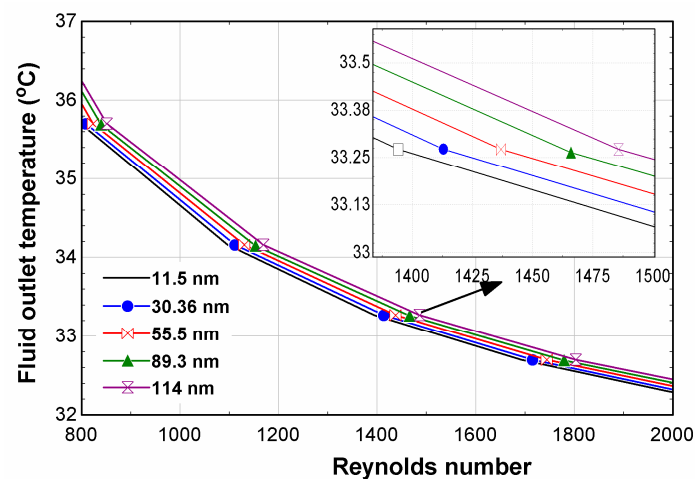


Figure 11. Fluid outlet temperature of the FPC.

On the other hand, it is vital to examine the pressure drop caused by the presence of the particles to provide a thorough assessment of the effectivity in the application of nanofluids. The pressure drop also has a huge effect on the pump work needed to move the fluid through the collector system [68]. Figure 12 shows the pressure drop increases with the Reynolds number increasing. This is attributed to the increase in the coefficient of friction between the fluid and the walls of the absorber. This is supported by several studies; a study by [69] showed that at a higher Reynolds number the pressure drop increases, and is also more significant for wavy pipes than for spiral pipes. Moreover, the difference in the pressure drop between the nanoparticle sizes was insignificant as compared to the higher Reynolds number. At a Reynolds number of 800, the percentage difference between the NPS of 11.5 and 114 nm was 12.5%, while at 2000, the percentage difference of the pressure drop between them was 17%. The pressure drop at the Reynolds numbers of 2000 for 11.5 nm, 30.36 nm, 55.5 nm, 89.3 nm, and 114 nm were 0.9 kPa, 0.87 kPa, 0.84 kPa, 0.804 kPa and 0.79 kPa. It is important to state that factors, such as volume concentration and temperature, have more significant effects on the pressure drop and pump work of the FPC. The results also show that the highest pressure drop was measured for the smaller-sized nanoparticles. This observation was attributed to the effect of the friction factor in the collector tubes. As seen in Equation (10), the total head loss directly affected the pressure

drop in the system. Moreover, the density of the fluids also determined the magnitude of the pressured drop. The viscosity of the fluid affected the friction factor; the results showed that the smaller-sized particles had higher viscosity properties.

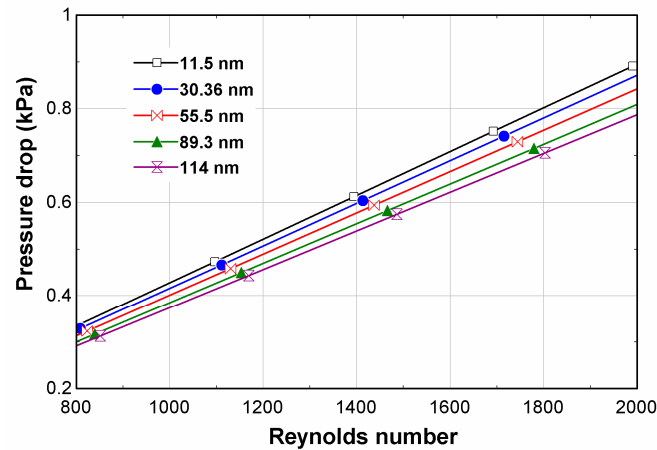


Figure 12. Pressure drop of the FPC.

Figure 13 shows that the pump work had a similar trend with the pressure drop. At a higher Reynolds number, the pumping power increased significantly. A maximum pump work of 0.114 W was calculated at a Reynolds number of 2000 for the 11.5 nm fly ash nanofluid. This impacts the cost of operating the collector system.

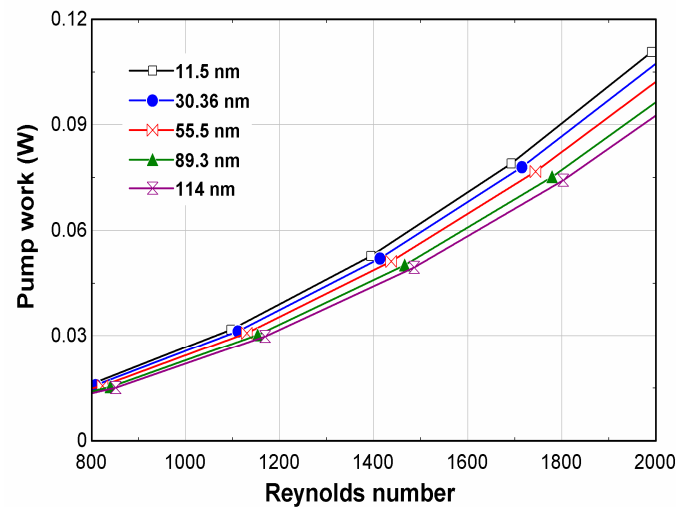


Figure 13. Pump work of the FPC.

For a more robust comparative analysis of the different NPS-based fly ash nanofluids, the performance evaluation criteria (PEC) analysis was carried out.

The computation of more general performance evaluation criteria, considering the pressure drop, mass flow rate, and temperature difference, is presented in Figure 14. The mathematical formulation used in computing the PEC is $PEC = \frac{mC_p\Delta T}{V\Delta P_t}$. Figure 14 shows a higher impact of the Reynolds number effect on the PEC values, though a similar trend of a better PEC of increasing the NPS is measured. At the lower Reynolds number, the difference in the PEC values of the different NPSs is more significant. At Reynolds numbers of 800, the PEC values of 11.5 nm, 30.36 nm, 55.5 nm, 89.3 nm, and 114 nm are 64.5, 66, 80, 86, and 88.

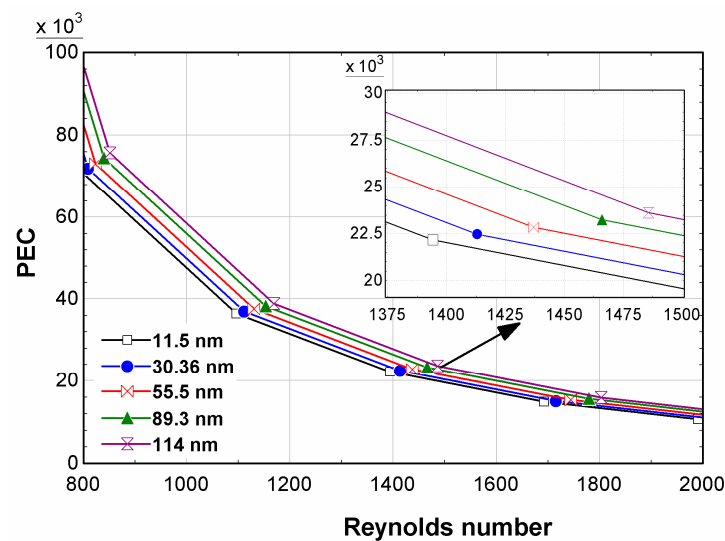


Figure 14. PECs of the FPCs at varying Reynolds numbers.

4. Conclusions

This study took a more specific research path in analyzing the influence of the nanoparticle size on the performance of a flat-plate collector. In the synthesis process of nanofluids (mono, hybrid, and ternary nanofluids), the morphology of the nanoparticles is of great importance, both in terms of their thermophysical properties and cost. This study validated the designed numerical model of a flat-plate collector, and then investigated the energy efficiency, exergy efficiency, mean plate and outlet temperature, pressure drop, pump work, and PEC parameters. This study also considered the laminar flow regime for all of the analyses. Some of the significant results obtained are:

- The maximum energy efficiency measured was 73.8%, which was recorded for the fly ash nanofluid with a nanoparticle size of 11.5 nm.
- The maximum energy efficiency of the 114 nm fly ash nanofluid was 73.5%, which was 0.41% less than the 11.5 nm NPS at a Reynolds number of 2000. At a Reynolds number of 800, the energy efficiencies of 11.5, 30.36, 55.5, 89.3, and 114 nm were 71.3%, 71%, 70.72%, 70.67%, and 70.5%.
- At a Reynolds number of 2000, the fly ash nanofluid with a nanoparticle size of 11.5 nm showed a top heat loss coefficient of 4.78 W/m²K, while the top heat loss coefficient of a NPS of 114 nm was 5.17 W/m²K.
- The numerical analysis measured the least and maximum mean plate temperatures at a Reynolds number of 2000 at 34.21 °C and 34.57 °C, respectively.
- At a higher Reynolds number, the pumping power increased significantly. A maximum pump work of 0.114 W was calculated at a Reynolds number of 2000 for the 11.5 nm fly ash nanofluid.

This study has significance. It considered a range of nanoparticle sizes that are frequently utilized in the literature for nanofluid synthesis; therefore, the results show a large range of inferences of the impact of the NPS on the performance of the FPC. However, future studies should include the effects of nanoparticle sizes of individual nanoparticles in hybrid and ternary nanofluids. A study by [70] explained the differing behaviors of hybrid nanofluids as a result of the differences in the nanoparticle sizes of the constituent nanoparticles in the composite. This phenomenon requires more research attention, especially in their application as working fluids in solar collector systems.

Author Contributions: Data curation, M.A.; Methodology, A.T.O. and M.A.; Project administration, M.D.; Supervision, D.K.; Writing—original draft, A.T.O. and Humphrey Adun; Writing—review & editing, H.A. and D.K. All authors have read and agreed to the published version of the manuscript.

Funding: This research received no external funding.

Institutional Review Board Statement: Not applicable.

Informed Consent Statement: Not applicable.

Data Availability Statement: Not applicable.

Conflicts of Interest: The authors declare no conflict of interest.

References

1. Curtin, J.; Mcinerney, C.; Gallachóir, B.Ó.; Hickey, C.; Deane, P.; Deeney, P. Quantifying stranding risk for fossil fuel assets and implications for renewable energy investment: A review of the literature. *Renew. Sustain. Energy Rev.* **2019**, *116*, 109402. [[CrossRef](#)]
2. Yang, X.; Pang, J.; Teng, F.; Gong, R.; Springer, C. The environmental co-benefit and economic impact of China ' s low-carbon pathways: Evidence from linking bottom-up and top-down models. *Renew. Sustain. Energy Rev.* **2021**, *136*, 110438. [[CrossRef](#)]
3. Al-maamary, H.M.S.; Kazem, H.A.; Chaichan, M.T. The impact of oil price fluctuations on common renewable energies in GCC countries. *Renew. Sustain. Energy Rev.* **2017**, *75*, 989–1007. [[CrossRef](#)]
4. Hawwash, A.A.; Abdel, A.K.; Nada, S.A.; Ookawara, S. Numerical Investigation and Experimental Verification of Performance Enhancement of Flat Plate Solar Collector Using Nanofluids. *Appl. Therm. Eng.* **2018**, *130*, 363–374. [[CrossRef](#)]
5. Chen, X.; Zhou, P.; Chen, M. Enhancing the solar absorption performance of nanoparticle suspensions by tuning the scattering effect and incident light location. *Int. J. Therm. Sci.* **2022**, *177*, 107547. [[CrossRef](#)]
6. Chen, X.; Wu, D.; Zhou, P.; Chen, M.; Yan, H. Modeling the solar absorption performance of Copper@Carbon core-shell nanoparticles. *J. Mater. Sci.* **2021**, *56*, 13659–13672. [[CrossRef](#)]
7. Chen, M.; Chen, X.; Wu, D. Solar Thermal Conversion of Plasmonic Nanofluids: Fundamentals and Applications. In *Advances in Microfluidics and Nanofluids*; IntechOpen: London, UK, 2021.
8. Qiu, L.; Zhu, N.; Feng, Y.; Michaelides, E.E.; Żyła, G.; Jing, D.; Zhang, X.; Norris, P.M.; Markides, C.N.; Mahian, O. A review of recent advances in thermophysical properties at the nanoscale: From solid state to colloids. *Phys. Rep.* **2019**, *843*, 1–81. [[CrossRef](#)]
9. Yu, W.; Xie, H. A Review on Nanofluids: Preparation, Stability Mechanisms, and Applications. *J. Nanomater.* **2012**, *2012*, 435873. [[CrossRef](#)]
10. Khanafer, K.; Vafai, K. A critical synthesis of thermophysical characteristics of nanofluids. *Int. J. Heat Mass Transf.* **2011**, *54*, 4410–4428. [[CrossRef](#)]
11. Kanchana, C.; Zhao, Y.; Siddheshwar, P.G. A comparative study of individual influences of suspended multiwalled carbon nanotubes and alumina nanoparticles on Rayleigh-Bénard convection in water. *Phys. Fluids* **2018**, *30*, 084101. [[CrossRef](#)]
12. Hassan, M.I.; Alzarooni, I.A.; Shatilla, Y. The Effect of Water-Based Nanofluid Incorporating Al₂O₃ Nanoparticles on Heat Pipe Performance. *Energy Procedia* **2015**, *75*, 3201–3206. [[CrossRef](#)]
13. Jeong, J.; Li, C.; Kwon, Y.; Lee, J.; Kim, S.H.; Yun, R. Particle shape effect on the viscosity and thermal conductivity of ZnO nanofluids. *Int. J. Refrig.* **2013**, *36*, 2233–2241. [[CrossRef](#)]
14. Singh, M.; Lara, S.; Tlali, S. Effects of size and shape on the specific heat, melting entropy and enthalpy of nanomaterials. *J. Taibah Univ. Sci.* **2017**, *11*, 922–929. [[CrossRef](#)]
15. Maheshwary, P.B.; Handa, C.C.; Nemade, K.R.; Chaudhary, S.R. Role of nanoparticle shape in enhancing the thermal conductivity of nanofluids. *Mater. Today Proc.* **2019**, *28*, 873–878. [[CrossRef](#)]
16. Ranga Babu, J.A.; Kumar, K.K.; Srinivasa Rao, S. State-of-art review on hybrid nanofluids. *Renew. Sustain. Energy Rev.* **2017**, *77*, 551–565. [[CrossRef](#)]
17. Jai, S.S.; Momin, M.; Nwaokocha, C.; Sharifpur, M.; Meyer, J.P. An empirical study on the persuasive particle size effects over the multi-physical properties of monophasic MWCNT-Al₂O₃ hybridized nanofluids. *J. Mol. Liq.* **2022**, *361*, 119668. [[CrossRef](#)]
18. Bai, J.; Hussein, D.; Fagiry, M.A.; Tlili, I. Numerical analysis and two-phase modeling of water Graphene Oxide nanofluid flow in the riser condensing tubes of the solar collector heat exchanger. *Sustain. Energy Technol. Assess.* **2022**, *53*, 102408. [[CrossRef](#)]
19. Mustafa, J.; Alqaed, S.; Sharifpur, M. Evaluation of energy efficiency, visualized energy, and production of environmental pollutants of a solar flat plate collector containing hybrid nanofluid. *Sustain. Energy Technol. Assess.* **2022**, *53*, 102399. [[CrossRef](#)]
20. Yurddaş, A.; Çerçi, Y.; Sarı Çavdar, P.; Bektaş, A. The effects of the use of hybrid and mono nanofluids on thermal performance in flat-plate solar collectors. *Environ. Prog. Sustain. Energy* **2022**, *41*, e13770. [[CrossRef](#)]
21. Gulzar, O.; Qayoum, A.; Gupta, R. Experimental study on stability and rheological behaviour of hybrid Al₂O₃-TiO₂ Therminol-55 nanofluids for concentrating solar collectors. *Powder Technol.* **2019**, *352*, 436–444. [[CrossRef](#)]
22. Gulzar, O.; Qayoum, A.; Gupta, R. Experimental study on thermal conductivity of mono and hybrid Al₂O₃-TiO₂ nanofluids for concentrating solar collectors. *Int. J. Energy Res.* **2021**, *45*, 4370–4384. [[CrossRef](#)]
23. Khetib, Y.; Abo-dief, H.M.; Alanazi, A.K.; Sajadi, S.M. Effect of nanoparticles shape on turbulent nanofluids flow within a solar collector by using hexagonal cross-section tubes. *Sustain. Energy Technol. Assess.* **2022**, *51*, 101843. [[CrossRef](#)]
24. Koblinski, P.; Eastman, J.A.; Cahill, D.G. Nanofluids for thermal transport. *Mater. Today* **2005**, *8*, 36–44. [[CrossRef](#)]
25. Kim, S.H.; Choi, S.R.; Kim, D. Thermal conductivity of metal-oxide nanofluids: Particle size dependence and effect of laser irradiation. *ASME 2012 Int. Mech. Eng. Congr. Expo.* **2007**, *129*, 298–307. [[CrossRef](#)]

26. Das, S.K. An experimental investigation into the thermal conductivity enhancement in oxide and metallic nanofluids. *J. Nanoparticle Res.* **2010**, *12*, 1015–1031. [[CrossRef](#)]
27. Hemmat Esfe, M.; Saedodin, S.; Wongwises, S.; Toghraie, D. An experimental study on the effect of diameter on thermal conductivity and dynamic viscosity of Fe/water nanofluids. *J. Therm. Anal. Calorim.* **2015**, *119*, 1817–1824. [[CrossRef](#)]
28. Xia, G.; Jiang, H.; Liu, R.; Zhai, Y. International Journal of Thermal Sciences Effects of surfactant on the stability and thermal conductivity of Al₂O₃/de-ionized water nano fluids. *Int. J. Therm. Sci.* **2014**, *84*, 118–124. [[CrossRef](#)]
29. Beck, M.P.; Yuan, Y.; Warriar, P.; Teja, A.S. The effect of particle size on the thermal conductivity of alumina nanofluids. *J. Nanoparticle Res.* **2009**, *11*, 1129–1136. [[CrossRef](#)]
30. Timofeeva, E.V.; Smith, D.S.; Yu, W.; France, D.M.; Singh, D.; Routbort, J.L. Particle size and interfacial effects on thermo-physical and heat transfer characteristics of water-based α -SiC nanofluids. *Nanotechnology* **2010**, *21*, 215703. [[CrossRef](#)]
31. He, Y.; Jin, Y.; Chen, H.; Ding, Y.; Cang, D.; Lu, H. Heat transfer and flow behaviour of aqueous suspensions of TiO₂ nanoparticles (nanofluids) flowing upward through a vertical pipe. *Int. J. Heat Mass Transf.* **2007**, *50*, 2272–2281. [[CrossRef](#)]
32. Turgut, A.; Tavman, I.; Chirtoc, M.; Schuchmann, H.P.; Sauter, C.; Tavman, S. Thermal Conductivity and Viscosity Measurements of Water-Based TiO₂ Nanofluids. *Int. J. Thermophys.* **2009**, *30*, 1213–1226. [[CrossRef](#)]
33. Nguyen, C.T.; Desgranges, F.; Roy, G.; Galanis, N.; Maré, T.; Boucher, S.; Angue Mintsa, H. Temperature and particle-size dependent viscosity data for water-based nanofluids—Hysteresis phenomenon. *Int. J. Heat Fluid Flow* **2007**, *28*, 1492–1506. [[CrossRef](#)]
34. Teng, T.; Hung, Y.; Teng, T.; Mo, H.; Hsu, H. The effect of alumina / water nano fluid particle size on thermal conductivity. *Appl. Therm. Eng.* **2010**, *30*, 2213–2218. [[CrossRef](#)]
35. Anoop, K.B.; Sundararajan, T.; Das, S.K. International Journal of Heat and Mass Transfer Effect of particle size on the convective heat transfer in nanofluid in the developing region. *Int. J. Heat Mass Transf.* **2009**, *52*, 2189–2195. [[CrossRef](#)]
36. Angayarkanni, S.A.; Sunny, V.; Philip, J. Effect of Nanoparticle Size, Morphology and Concentration on Specific Heat Capacity and Thermal Conductivity of Nanofluids. *J. Nanofluids* **2015**, *4*, 302–309. [[CrossRef](#)]
37. Dudda, B.; Shin, D. Effect of nanoparticle dispersion on specific heat capacity of a binary nitrate salt eutectic for concentrated solar power applications. *Int. J. Therm. Sci.* **2013**, *69*, 37–42. [[CrossRef](#)]
38. Riazi, H.; Mesgari, S.; Ahmed, N.A.; Taylor, R.A. The effect of nanoparticle morphology on the specific heat of nanosalts. *Int. J. Heat Mass Transf.* **2016**, *94*, 254–261. [[CrossRef](#)]
39. Tiznobaik, H.; Shin, D. Enhanced specific heat capacity of high-temperature molten salt-based nanofluids. *Int. J. Heat Mass Transf.* **2013**, *57*, 542–548. [[CrossRef](#)]
40. Seo, J.; Shin, D. Size effect of nanoparticle on specific heat in a ternary nitrate (LiNO₃-NaNO₃-KNO₃) salt eutectic for thermal energy storage. *Appl. Therm. Eng.* **2016**, *102*, 144–148. [[CrossRef](#)]
41. Dhairiyasamy, R.; Saleh, B.; Govindasamy, M.; Ayman, A.; Afzal, A.; Abdelrhman, Y. Effect of particle size on thermophysical and heat transfer properties of Ag nanofluid in a radiator—An experimental investigation. *Inorg. Nano-Metal Chem.* **2021**, 1–15. [[CrossRef](#)]
42. Amin, T.E.; Roghayeh, G.; Fatemeh, R.; Fatollah, P. Evaluation of nanoparticle shape effect on a nanofluid based flat-plate solar collector efficiency. *Energy Explor. Exploit.* **2015**, *33*, 659–676. [[CrossRef](#)]
43. Yousefi, T.; Shojaeizadeh, E.; Veysi, F.; Zinadini, S. An experimental investigation on the effect of pH variation of MWCNT-H₂O nanofluid on the efficiency of a flat-plate solar collector. *Sol. Energy* **2012**, *86*, 771–779. [[CrossRef](#)]
44. Kanti, P.; Sharma, K.V.; Raja Sekhar, Y. Influence of particle size on thermal conductivity and dynamic viscosity of water—Based Indian coal fly ash nanofluid. *Heat Transf.* **2021**, *51*, 413–433. [[CrossRef](#)]
45. Verma, S.K.; Tiwari, A.K.; Chauhan, D.S. Experimental evaluation of flat plate solar collector using nanofluids. *Energy Convers. Manag.* **2017**, *134*, 103–115. [[CrossRef](#)]
46. Faizal, M.; Saidur, R.; Mekhilef, S.; Alim, M.A. Energy, economic and environmental analysis of metal oxides nanofluid for flat-plate solar collector. *Energy Convers. Manag.* **2013**, *76*, 162–168. [[CrossRef](#)]
47. Said, Z.; Saidur, R.; Sabiha, M.A.; Rahim, N.A.; Anisur, M.R. ScienceDirect Thermophysical properties of Single Wall Carbon Nanotubes and its effect on exergy efficiency of a flat plate solar collector. *Sol. Energy* **2015**, *115*, 757–769. [[CrossRef](#)]
48. Youse, T.; Veysi, F.; Shojaeizadeh, E.; Zinadini, S. An experimental investigation on the effect of Al₂O₃-H₂O nano fluid on the efficiency of flat-plate solar collectors. *Renew. Energy* **2012**, *39*, 293–298. [[CrossRef](#)]
49. Sarsam, W.S.; Kazi, S.N.; Badarudin, A. Thermal performance of a flat-plate solar collector using aqueous colloidal dispersions of multi-walled carbon nanotubes with different outside diameters. *Exp. Heat Transf.* **2022**, *35*, 258–281. [[CrossRef](#)]
50. Dobriyal, R.; Negi, P.; Sengar, N.; Singh, D.B. Materials Today: Proceedings A brief review on solar flat plate collector by incorporating the effect of nanofluid. *Mater. Today Proc.* **2020**, *21*, 1653–1658. [[CrossRef](#)]
51. Yazdanifard, F.; Ebrahimnia-Bajestan, E.; Ameri, M. Investigating the performance of a water-based photovoltaic/thermal (PV/T) collector in laminar and turbulent flow regime. *Renew. Energy* **2016**, *99*, 295–306. [[CrossRef](#)]
52. Duffie, J.A.; Beckman, W.A.; Blair, N. *Solar Engineering of Thermal Processes, Photovoltaics and Wind*; John Wiley & Sons: Hoboken, NJ, USA, 2020.
53. Dominguez, J. *Solar Energy Engineering Processes and Systems*, 2nd ed.; Academic Press: Cambridge, MA, USA, 2017.
54. Said, Z.; Sabiha, M.A.; Saidur, R.; Hepbasli, A.; Rahim, N.A.; Mekhilef, S.; Ward, T.A. Performance enhancement of a Flat Plate Solar collector using Titanium dioxide nanofluid and Polyethylene Glycol dispersant. *J. Clean. Prod.* **2015**, *92*, 343–353. [[CrossRef](#)]

55. Çengel, A.Y.; Cimbala, M.J. *Fluid Mechanics: Fundamentals and Applications*, 2nd ed.; McGraw-Hill Higher Education: New York, NY, USA, 2009.
56. Kumar, V.; Sarkar, J. Particle ratio optimization of Al₂O₃-MWCNT hybrid nanofluid in minichannel heat sink for best hydrothermal performance. *Appl. Therm. Eng.* **2020**, *165*, 114546. [[CrossRef](#)]
57. Adun, H.; Mukhtar, M.; Adedeji, M.; Agwa, T.; Ibrahim, K.H.; Bamisile, O.; Dagbasi, M. Synthesis and Application of Ternary Nanofluid for Photovoltaic-Thermal System: Comparative Analysis of Energy and Exergy Performance with Single and Hybrid Nanofluids. *Energies* **2021**, *14*, 4434. [[CrossRef](#)]
58. Prahald, A.K.; Soukup, J.M.; Inmon, J.; Willis, R.; Ghio, A.J.; Becker, S.; Gallagher, J.E. Ambient air particles: Effects on cellular oxidant radical generation in relation to particulate elemental chemistry. *Toxicol. Appl. Pharmacol.* **1999**, *158*, 81–91. [[CrossRef](#)] [[PubMed](#)]
59. Dwivedi, S.; Saquib, Q.; Al-Khedhairi, A.A.; Ali, A.Y.S.; Musarrat, J. Characterization of coal fly ash nanoparticles and induced oxidative DNA damage in human peripheral blood mononuclear cells. *Sci. Total Environ.* **2012**, *437*, 331–338. [[CrossRef](#)]
60. Jang, S.P.; Choi, S.U.S. Role of Brownian motion in the enhanced thermal conductivity of nanofluids. *Appl. Phys. Lett.* **2004**, *84*, 4316–4318. [[CrossRef](#)]
61. Asadi, A.; Alarif, I.M.; Ali, V.; Nguyen, H.M. An experimental investigation on the effects of ultrasonication time on stability and thermal conductivity of MWCNT-water nanofluid: Finding the optimum ultrasonication time. *Ultrason. Sonochem.* **2019**, *58*, 104639. [[CrossRef](#)]
62. Akram, N.; Montazer, E.; Kazi, S.N.; Elahi, M.; Soudagar, M.; Ahmed, W.; Nashrul, M.; Zubir, M.; Afzal, A.; Ridha, M.; et al. Experimental investigations of the performance of a flat-plate solar collector using carbon and metal oxides based nanofluids. *Energy* **2021**, *227*, 120452. [[CrossRef](#)]
63. Gulzar, O.; Qayoum, A.; Gupta, R. Photo-thermal characteristics of hybrid nanofluids based on Therminol-55 oil for concentrating solar collectors. *Appl. Nanosci.* **2019**, *9*, 1133–1143. [[CrossRef](#)]
64. Prasher, R.; Bhattacharya, P.; Phelan, P.E. Thermal conductivity of nanoscale colloidal solutions (nanofluids). *Phys. Rev. Lett.* **2005**, *94*, 025901. [[CrossRef](#)]
65. Malvi, C.S.; Gupta, A.; Gaur, M.K.; Crook, R.; Dixon-Hardy, D.W. Experimental investigation of heat removal factor in solar flat plate collector for various flow configurations. *Int. J. Green Energy* **2017**, *14*, 442–448. [[CrossRef](#)]
66. Okonkwo, E.C.; Wole-Osho, I.; Kavaz, D.; Abid, M.; Al-Ansari, T. Thermodynamic evaluation and optimization of a flat plate collector operating with alumina and iron mono and hybrid nanofluids. *Sustain. Energy Technol. Assess.* **2020**, *37*, 100636. [[CrossRef](#)]
67. Mahian, O.; Kianifar, A.; Sahin, A.Z.; Wongwises, S. International Journal of Heat and Mass Transfer Entropy generation during Al₂O₃/water nanofluid flow in a solar collector: Effects of tube roughness, nanoparticle size, and different thermophysical models. *Int. J. Heat Mass Transf.* **2014**, *78*, 64–75. [[CrossRef](#)]
68. Brottier, L.; Brottier, L.; Bennacer, R. Pressure Drop in Parallel Flow Flat-Plate PVT Collectors. *ISES* **2017**, 1–11. [[CrossRef](#)]
69. Reza, M.; Moravej, M.; Hossein, M. Heat transfer enhancement in a flat plate solar collector with different flow path shapes using nanofluid. *Renew. Energy* **2020**, *146*, 2316–2329. [[CrossRef](#)]
70. Wole-osh, I.; Okonkwo, E.C.; Kavaz, D.; Abbasoglu, S. An experimental investigation into the effect of particle mixture ratio on specific heat capacity and dynamic viscosity of Al₂O₃-ZnO hybrid nanofluids. *Powder Technol.* **2020**, *363*, 699–716. [[CrossRef](#)]